AIP | Journal of Applied Physics

Dynamics and density distributions in a capillary-discharge waveguide with an embedded supersonic jet

N. H. Matlis, A. J. Gonsalves, S. Steinke, J. van Tilborg, E. H. Matlis, B. Shaw, D. E. Mittelberger, C. G. R. Geddes, and W. P. Leemans

Citation: Journal of Applied Physics **118**, 204506 (2015); doi: 10.1063/1.4935631
View online: http://dx.doi.org/10.1063/1.4935631
View Table of Contents: http://scitation.aip.org/content/aip/journal/jap/118/20?ver=pdfcov
Published by the AIP Publishing

JOURNAL OF APPLIED PHYSICS **118**, 204506 (2015)

Dynamics and density distributions in a capillary-discharge waveguide with an embedded supersonic jet

N. H. Matlis,[1,a)] A. J. Gonsalves,[1] S. Steinke,[1] J. van Tilborg,[1] E. H. Matlis,[2] B. Shaw,[1] D. E. Mittelberger,[1] C. G. R. Geddes,[1] and W. P. Leemans[1,3]
[1]*Lawrence Berkeley National Laboratory, Berkeley, California 94720, USA*
[2]*Department of Aerospace and Mechanical Engineering, University of Notre Dame, Notre Dame, Indiana 46556, USA*
[3]*Department of Physics, University of California, Berkeley, California 94720, USA*

(Received 6 July 2015; accepted 31 October 2015; published online 25 November 2015)

We present an analysis of the gas dynamics and density distributions within a capillary-discharge waveguide with an embedded supersonic jet. This device provides a target for a laser plasma accelerator which uses longitudinal structuring of the gas-density profile to enable control of electron trapping and acceleration. The functionality of the device depends sensitively on the details of the density profile, which are determined by the interaction between the pulsed gas in the jet and the continuously-flowing gas in the capillary. These dynamics are captured by spatially resolving recombination light from several emission lines of the plasma as a function of the delay between the jet and the discharge. We provide a phenomenological description of the gas dynamics as well as a quantitative evaluation of the density evolution. In particular, we show that the pressure difference between the jet and the capillary defines three regimes of operation with qualitatively different longitudinal density profiles and show that jet timing provides a sensitive method for tuning between these regimes. © *2015 AIP Publishing LLC*. [http://dx.doi.org/10.1063/1.4935631]

I. INTRODUCTION

Laser plasma accelerators (LPAs) are gaining increasing visibility as attractive electron sources because of their ultra-high acceleration gradients which make them extremely compact.[1–5] The unique properties of LPAs, including high peak brightness, femtosecond bunch durations, and intrinsic synchronization to the laser system, promise to enable a wide variety of new, exciting, table-top-scale applications ranging from high-energy physics to medicine to ultrafast science.[6–10] The high acceleration gradients are achieved by using relativistically-intense laser pulses to excite electron-density waves in a plasma which yield ∼GV/cm electrostatic fields that are thousands of times higher than can be achieved in RF-based conventional accelerators. Due to the highly nonlinear nature of this process, however, LPAs currently suffer from large energy spreads, difficulties in tuning parameters, and a high degree of shot-to-shot variability relative to their RF counterparts. Managing the dynamics of the laser-plasma interaction is thus a critical step for the implementation of this technology, and has been a focus of LPA research over the last decade. Of primary importance are controlling the mechanisms of injection and subsequent acceleration.

Laser-machined, gas-filled, capillary-discharge waveguides are very attractive targets to address this need for several reasons. First, the waveguide keeps the laser focused, thereby increasing the acceleration length and permitting higher beam energies with lower driver input energies relative to unguided LPAs.[11,12] Second, they provide a versatile platform for compact implementation of longitudinal density structuring, i.e., controlling the longitudinal profile of the plasma density to tailor the properties of the accelerator. In particular, the integration of a sub-mm, supersonic jet into the design provides a tunable and localized region of high density which has recently been shown to be effective for enhancing stability and for controlling electron injection and energy.[13,14]

Despite the success of this approach, precise characterization of the device behavior, including quantification of the jet pressure, its effect on the rest of the structure, and the temporal evolution of the system, has not been possible due to the lack of a suitable diagnostic. Standard plasma-density diagnostics based on interferometry cannot be used here because of the scattering at the laser-machined surfaces and the lack of cylindrical symmetry.[15] Since the jet must be pulsed in order to maintain sufficiently low background gas densities, the device exhibits a highly dynamic and complex behavior, resulting from the jet-capillary interaction. An understanding of these phenomena is critical for guiding further improvements in the device design, including the location and shape of the jet nozzle, as well as for development of a consistent methodology to optimize the device performance. In particular, the jet-pressure evolution and the induced, transient density gradients within the structure must be characterized to effectively control the target density profile.

In this paper, we outline the sequence of gas-dynamic events involved in the jet-pulsing cycle and show how to use the evolution of the gas distributions within the device to quantify both the jet-pressure as a function of time as well as the resulting density gradients. Analytical calculations based on simple fluid models are used to validate the experimentally-determined dynamics. In particular, we show that pressure

[a)]Electronic mail: nmatlis@gmail.com

gradients induced in the capillary by the jet are concentrated in the region connecting the jet to the rest of the capillary, and that the gradients in that region can be tuned from negative to positive using the jet timing. Three timing regimes, defined by the sign of the gradient, are described, and estimates of the longitudinal gas-density profiles in these three regimes, based on the ideal gas law, are presented along with their impact on the operation of the device.

II. EXPERIMENTAL SETUP

Experiments were performed in the BELLA center at Lawrence Berkeley National Laboratory. A 250 μm diameter capillary waveguide and supersonic jet nozzle were laser-machined onto sapphire plates using an on-site facility,[13] producing structures with a surface roughness of about 10 μm, peak to valley. Figure 1(a) shows the sapphire structure as well as the discharge and gas-delivery hardware. Each of the functionally-distinct regions of the sapphire structure referred to in the text have been independently labeled in the figure. A continuous-flow controller at pressure $P_{H_2} = 50 - 200$ Torr was used to supply hydrogen (H_2) gas to the capillary via two curved slots of cross-sectional area 0.5 mm^2 which intersected the capillary 25 mm apart. The supersonic converging-diverging (CD) nozzle, with a throat diameter of 570 μm and a 6° expansion cone, was machined transversely to the capillary between the capillary entrance and the first fill slot. The capillary intersected the expansion section 1.2 mm from the throat, where the cross-sectional area was approximately twice that at the throat.

A high-speed valve supplied by Alameda Applied Sciences Corporation[16] with an open time of 1 ms was used to pulse helium (He) with pressure $P_{He} = 0 - 50$ psi (gauge) into a "plenum" which supplied the backing pressure for the nozzle. The plenum consisted of a section of 3/16-in. inner diameter pneumatic tubing, the jet supply slot, and various connectors. An independently-pumped exhaust channel connected to the end of the nozzle was used to evacuate and ensure supersonic operation of the jet.

The condition to reach supersonic operation[17] (i.e., choked flow) for ideal monoatomic gases like He, which have an adiabatic index of $\gamma = 5/3$, is $P_{amb}/P_{He} < 0.487$, where P_{amb} is the ambient pressure in the nozzle before the jet fires. Assuming there is sufficient time between shots for the plenum to evacuate through the exhaust, the plenum pressure is caused by a small amount of H_2 which leaks into the plenum from the capillary. It is therefore clear that $P_{amb} < P_{H_2} \ll P_{He}$, and that the nozzle is supersonic for all combinations of P_{He} and P_{H_2} used here.

A 100–150 A, 200 ns current pulse was used to ionize gas in the capillary and jet to form the optical waveguide.[11] The resultant plasma volume extended up the capillary fill slots as well as the jet supply and down the jet exhaust. A custom spectrometer was implemented by imaging the sapphire structure from the side using a CCD camera with a 50 mm TV-objective lens and placing a transmission grating in between the lens and the object (Fig. 1(b)). The wavelength selection was done by rotating the camera about a horizontal axis lying in the plane of the transmission grating.

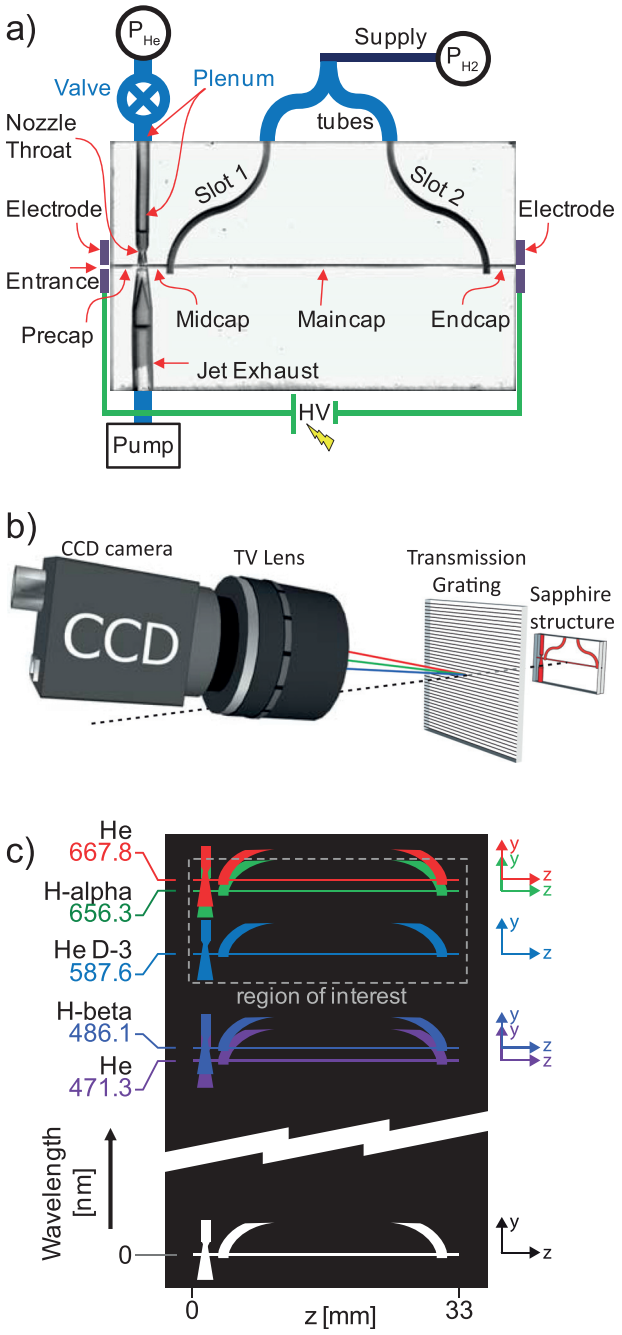

FIG. 1. (a) Diagram of the integrated capillary waveguide and supersonic jet structure. (b) Schematic of spectrometer. Three diffracted rays of red, green, and blue represent dispersion of the light from the sapphire structure. (c) Conceptual depiction of the image plane showing sapphire structure multiply represented by several hydrogen and helium lines. The dashed box labeled "region of interest" shows the analysis region.

The result was to create an angularly-dispersed set of images, with one image for each emission wavelength (Fig. 1(c)). The transmission grating was oriented to disperse light vertically so that the vertical direction in the image plane corresponded simultaneously to wavelength and (locally to each image) the vertical spatial dimension. Interpretation of the vertical image direction thus required special treatment.

In the ideal concept of the spectrometer, the emission lines are sufficiently narrow and spectrally separated that each one generates a single, spatially resolved image in a

vertical location distinct from the other lines. In this way, 2D spatial information can be obtained for each emission line. In practice, however, there were several deviations from this ideal. First, there were adjacent lines in the combined He-H_2 spectra that were close enough to each other to cause partial overlap of their images (See Fig. 1(c)). Second, for the H_2 lines (in particular, in the region of the capillary), the spectra were significantly broadened, causing blurring of features in the vertical direction. And third, a continuum emission existed in between the distinct atomic lines that contributed to a background signal on the camera.

The negative effects of image-overlap and spectral-blurring were mostly confined to the vertically-extended components of the structure, such as the jet, the jet exhaust, and the gas slots. Therefore, the quantitative analysis was done with light coming exclusively from various sections of the capillary. Since the transverse dimension of the capillary was too small to be resolved by the imaging system, the vertical direction for this component could be interpreted unambiguously as wavelength, and since there was no dispersion in the horizontal direction, longitudinal variations could be resolved. The use of distinct gases for the jet and capillary (i.e., He and H_2, respectively) was done specifically to allow the two sources to be distinguished by their emission signature and for the dynamics to, therefore, be resolved. The spectrometer was set up to capture multiple hydrogen and helium emission lines to allow calibration of the spectral axis. Figure 2 shows three individual raw images cropped to display the region of interest (Fig. 1(c)), which included the 2D brightness distributions of the H_α (656.3 nm) and helium D_3 (587.6 nm) emission lines which were used for the analysis. The three images were chosen to illustrate the main features of the evolution of the 2D brightness distributions and show the relationship between hydrogen-line and helium-line distributions. A more in-depth description of the three images is provided in the analysis below.

The time resolution of the technique was set by the recombination time of the plasma, which was measured to be of the same order as the duration of the current pulse, i.e., 200–300 ns. Because the recombination time is much shorter than the timescales of fluid motion, the light acted as a strobe to capture the (effectively) instantaneous spatial distributions of the neutral He and H_2. The dynamics of the interaction between the two gases was thus captured by scanning the timing delay, t, between the discharge and the jet trigger.

Interpretation of the measured line-intensity distributions is complicated by their dependence on several parameters which can each vary spatially, including the neutral gas density, the degree of ionization, the plasma temperature, the collection efficiency of the imaging optics, and the output coupling of the recombination light (i.e., the transmission through the structure walls), which is affected by the surface roughness as well as the presence of depositions, for example, from materials used in the assembly of the device. In addition, the line brightness and its longitudinal profile were observed to vary on a timescale of thousands of shots, most likely due to evolution of the output coupling, although no significant modification of the surface roughness was detected. Establishment of a suitable reference is thus a key aspect of the analysis required to obtain quantitative information about the jet-capillary dynamics.

III. ANALYSIS

In this section, we describe an intricate series of steps for quantifying the pressure evolution and gradients within the device. To clarify the methodology, we first present an overview of the neutral-gas evolution, resulting from the interaction between the jet and capillary gases. A detailed description of each step then follows.

Before the jet fires, H_2 flows in a steady state through the fill slots to the capillary and then through the Endcap and Midcap. The fill slots and other H_2 delivery tubes were designed to minimize the difference between the pressure at the source, P_{H_2}, and the pressure at the capillary, P_{cap}, resulting in $P_{cap} \approx P_{H_2}$, to within about 1%. Since the pressure supplied by both slots is the same, there is no flow across the Maincap, and thus a region of constant density is provided. The flow through the Midcap and Endcap, however, results in pressure and density gradients in these sections.[18,19] Most of the gas exiting the Midcap flows down the jet exhaust rather than into the Precap, due to the former's much-larger diameter. Figure 2(a) shows a spectrometer image taken just before the jet fires. The H_2 emission line is visible,

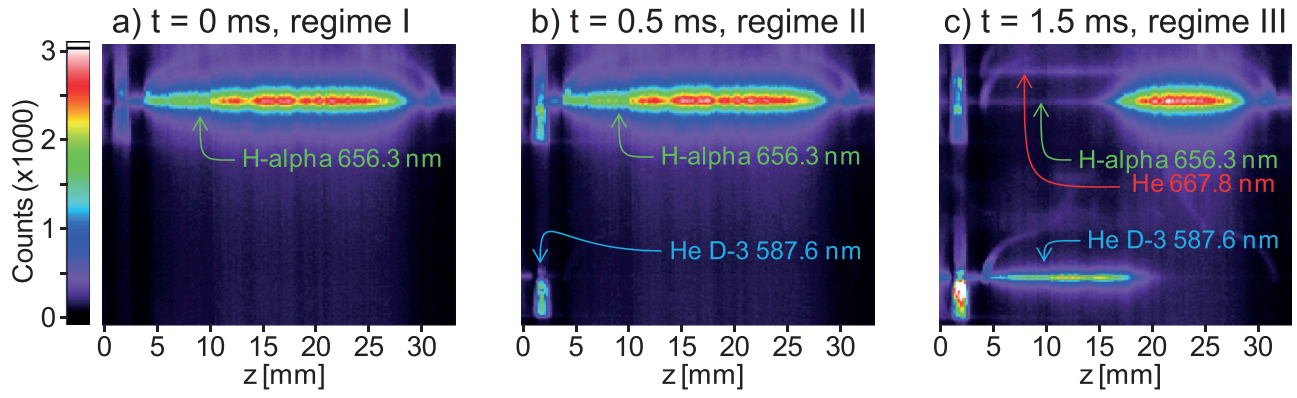

FIG. 2. (a)–(c) Spectrometer images corresponding to region of interest in Fig. 1(c), showing the hydrogen H_α (656.3 nm) and helium D_3 (587.6 nm) emission lines for discharge delays of 0 ms, 0.5 ms, and 1.5 ms, respectively, at $P_{He} = 65$ psi (absolute) and $P_{H_2} = 100$ Torr.

illuminating the entire structure, while the He line is completely absent. The longitudinal variations in the H_2-line brightness are caused by variations in both the output coupling and the light collection efficiency.

Once the valve triggers, high-pressure He rushes into the plenum, filling it on a ~1 ms timescale. If the valve is open sufficiently long, the plenum pressure equilibrates with the source pressure, P_{He}, since the valve orifice is much larger than the nozzle orifice. Once the valve closes, the plenum pressure then drops as gas escapes through the nozzle orifice. The jet pressure, $P_{jet}(t)$, corresponding to the pressure in the nozzle where it intersects the capillary, tracks the evolution of the plenum pressure, but is significantly lower due to the effects of expansion in the nozzle. The pressure gradient in the Midcap reacts in turn to the evolving jet pressure. As the jet pressure rises at the beginning of the cycle, the pressure difference across the Midcap, $\Delta P(t) \equiv P_{jet}(t) - P_{cap}$, becomes less negative and eventually changes sign after going through zero. The direction of the flow and the density gradient also reverse during this process. Once the flow reverses, He from the jet progressively displaces the H_2, first in the Midcap and then in the Maincap and fill slots. Figure 2(b) shows a spectrometer image at the moment $P_{jet}(t) = P_{cap}$. The H_2-line distribution is relatively unchanged, compared to Figure 2(a), but the He line has now appeared, localized to the jet, the jet exhaust and the Precap. In Figure 2(c), P_{jet} has exceeded P_{cap}, and the displacement of H_2 by He can be seen by the extension of the He line into the Maincap and by the corresponding regression of the H_2 line. Once the valve closes, P_{jet} begins to drop and eventually falls below P_{cap}, at which point the gas flows revert to their original directions. However, any He which entered the Maincap remains trapped, at this point, by the H_2 flowing through the slots.

The relationship between $P_{jet}(t)$ and P_{cap} thus defines three regimes with qualitatively different behaviors and longitudinal gas-density distributions (Fig. 3). We label these regimes *sub-critical* ($P_{jet} < P_{cap}$), *critical* ($P_{jet} = P_{cap}$), and *over-critical* ($P_{jet} > P_{cap}$). It is assumed for the analysis here that P_{He} is sufficiently high that all three regimes are eventually reached, however, this is not always the case. During the evolution, the jet density and the positive gradient in the Precap both track the jet pressure monotonically. By contrast, the density gradient in the Midcap tracks the pressure difference, $\Delta P(t)$, which reverses sign during the evolution of the jet. In the Maincap, the density gradient remains zero until the over-critical regime is reached, at which point a small negative gradient is generated. As described below, most of the pressure drop to the right of the jet occurs across the Midcap, and only about 6% occurs across the Maincap.

Because the jet pressure temporal evolution drives the dynamics of the system, quantitative determination of $P_{jet}(t)$ is the required first step of the analysis. In the second step, $P_{jet}(t)$ is used to model the displacement of H_2 by He in the over-critical regime in order to calibrate the flow properties of the system, which then allows a detailed description to be made for the longitudinal density profiles in each of the three regimes. The impacts of these density profiles on the operation of the accelerator are then discussed.

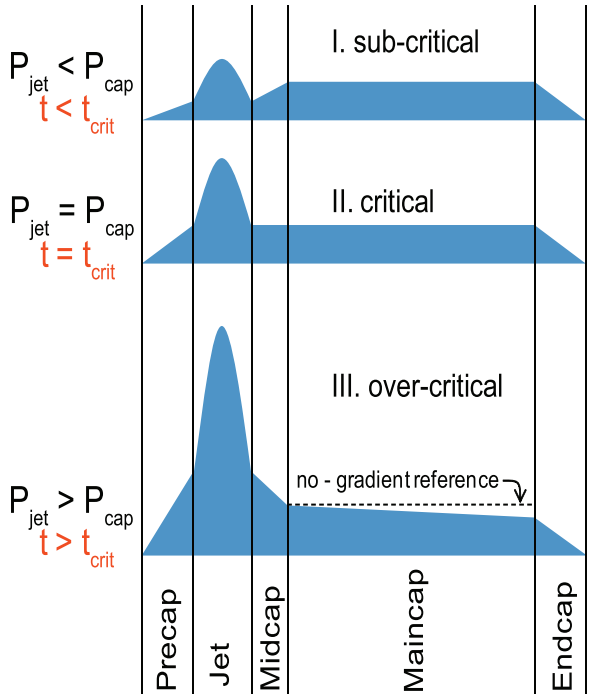

FIG. 3. Evolution of the longitudinal density profile resulting from the jet-pressure evolution through the three regimes.

A. Jet pressure evolution

The jet pressure evolution was characterized using the methodology presented by Matlis *et al.*,[20] and is summarized here. In that work, it was shown that the He emission light integrated over the region of the Precap, $S^{He}_{Precap}(t)$ (Fig. 4(a)), is proportional to the instantaneous jet pressure, $P_{jet}(t)$. Since the Precap is oriented transversely to the motion of the jet gas, it provides a measurement of the jet static pressure, which is directly connected to the density via the ideal gas law. Because the jet exhaust isolates the Precap from the rest of the capillary structure, the signal from Precap is unaffected by the capillary pressure or by the interaction between the jet and the capillary.

The calibration for $S^{He}_{Precap}(t)$ was obtained by using the Midcap as a sensor of the pressure balance between the jet and capillary. The integrated He signal from the Midcap (Fig. 4(a), red-solid curve) shows a sharp upward transition which defines the time, $t = t_{crit}$, when the jet pressure equals the capillary pressure ($P_{jet} = P_{cap}$). The H_2 signal integrated over the Midcap (Fig. 4(a), green-dotted curve) shows a corresponding sharp downward transition at the same time, indicating that the H_2 gets displaced by the He. Since $P_{cap} \approx P_{H_2}$, the pressure of the jet at the critical time, $P_{jet}(t_{crit})$, could be approximated by the known H_2 set pressure, P_{H_2}. The transition analysis thus provided a direct measurement of both a time and a pressure which define a reference point on the $P_{jet}(t)$ curve. The delay scan was then repeated for a range of capillary pressures (Fig. 4(b)). Since it takes longer to reach the critical condition for higher capillary pressures, the variation in t_{crit} with P_{H2} was used to map out $P_{jet}(t)$. By scaling $S^{He}_{Precap}(t)$ to fit this transition-based data, the desired calibration was then obtained (Fig. 4(c)). The calibrated $P_{jet}(t)$ curve agrees very

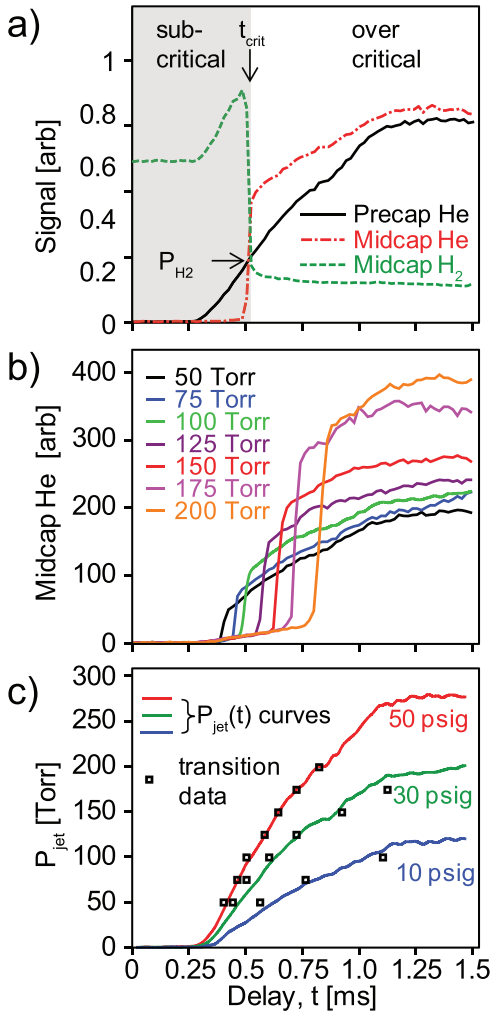

FIG. 4. Jet pressure calibration data taken in delay increments of 0.02 ms and averaged over three shots taken per step. (a) Sample data (P_{H_2} = 100 Torr and P_{He} = 50 psi (gauge)) used for determination of t_{crit} and calibration of $P_{jet}(t)$, showing the relationship between the Precap He (black solid line), the Midcap He (red dotted-dashed line), and the Midcap H_2 (green dashed line) signals. The level of the Precap He signal at t_{crit} corresponds to P_{H_2}. (b) Multiple Midcap He traces for P_{H_2} = 50, 75, 100, 125, 150, 175, 200 Torr and P_{He} = 50 psi (gauge), showing how t_{crit} increases with P_{H_2}. (c) Calibrated He pressure curves for P_{He} = 10, 30, 50 psi (gauge), overlapped with data from transition analysis (empty squares).

well with the transition-based data in both shape and absolute timing.

The plateau at the top of the $P_{jet}(t)$ curve shows that the plenum pressure, P_{plen}, has equilibrated to the source pressure, P_{He}, which enables a measurement of the pressure drop caused by the CD nozzle: $(P_{jet}/P_{plen})_{meas} = 0.085$. For comparison, an estimate of the pressure ratio[27] based on an isentropic expansion of 2.1, determined for our geometry, yields $(P_{jet}/P_{plen})_{isent} = 0.062$. The pressure ratio can then be used to determine the jet temperature based on isentropic expansion of an ideal gas

$$\frac{T_{jet}}{T_{plen}} = \left(\frac{P_{jet}}{P_{plen}}\right)^{\frac{\gamma-1}{\gamma}}. \quad (1)$$

Assuming the He is initially at room temperature, the jet temperature was then T_{jet} = 111 K.

B. Hagen-Poiseuille flow in the over-critical regime

The calibrated $P_{jet}(t)$ information was then used to characterize the longitudinal density distribution in the remainder of the capillary structure. Of particular importance to the operation of the device is the evolution of the density gradients in the Midcap and Maincap, which affect electron injection and subsequent acceleration in the LPA. To determine these gradients, a model was developed to explain the displacement of H_2 by He in the Maincap in the over-critical regime. Comparison of the model to the observed displacement allowed calibration of the pressure gradients in the Midcap and Maincap, from which the density gradients could then be inferred using the ideal gas law.

The flow in the Maincap was resolved by plotting the longitudinal intensity distributions of the He and H_2 emission lines (integrated over the transverse dimension of the capillary) as a function of the discharge delay (Fig. 5). The longitudinal intensity distributions of the emission lines were normalized using the distributions at early times before the jet arrival. As a result, the longitudinal variations due to

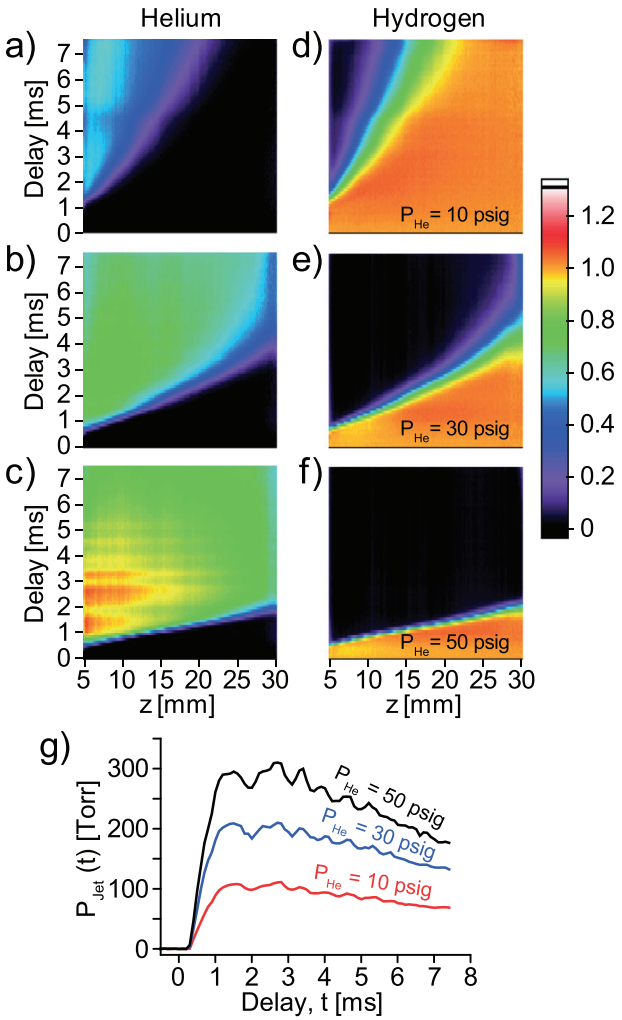

FIG. 5. (a)–(c) Plots of the helium D_3 emission-line longitudinal distribution vs delay for P_{He} = 10, 30, 50 psi (gauge), respectively, and P_{H_2} = 85 Torr. (d)–(f) Corresponding hydrogen H_α emission-line plots. Each horizontal line in the images in (a)–(f) corresponds to a single step of 0.100 ms in the delay scan, and is average over the data taken from the three images in that step. (g) Calibrated $P_{jet}(t)$ curves associated with (a)–(f).

non-flow-related factors, noticeable, for example, in Fig. 2, were eliminated. The progressive advancement and the complementing retreat of the He and H_2 line distributions, respectively, show that He leaks into the capillary and nearly completely displaces the H_2. The flow rate is only a few m/s and depends roughly linearly on P_{He} and P_{H_2}.

The very low Knudsen and Reynolds numbers (Kn ≈ 0.006 and Re ≈ 1, respectively), indicate that the flow is both viscous and laminar, suggesting that it can be described by Hagen-Poiseuille (H-P) flow, for which pressure gradients are balanced by viscous friction, resulting in a constant flow with a parabolic radial flow profile.[17,21] The flow deviates from traditional H-P flow, however, in that it is compressible, it is made up of two gas components, and the pressure gradient varies in time. Compressibility may be neglected since the mean free path is much smaller than the pipe diameter[21] (i.e., Kn $\ll 1$) and the flow is very subsonic: $\bar{u} \ll c_s$, where c_s is the sound speed. The presence of more than one gas species was accounted for by using the weighted average of the viscosity of each gas component, and the evolution of pressure gradient was handled by assuming that the flow was quasi-static.

The quasi-static assumption is valid provided that the flow in the device responds on a time-scale significantly faster than the variation in the jet pressure. Two time-scales of particular relevance are the formation time, which describes how quickly H-P flow is established, and the time-scale for the pressure variations to be communicated to the rest of the device. The formation time was estimated to be $t_{form} = R\mathrm{Re}/15\bar{u} \approx 8\mu$s, where R is the pipe radius,[22,23] which is much faster than the fastest variations in $P_{jet}(t)$ (i.e., the onset of the jet, $t_{onset} \approx 750\mu$s—see Fig. 4(c)). The time-scale for the jet-pressure variations to be communicated to the entire structure can be inferred from the horizontal striations visible, for example, in Figure 5(c). These striations are due to pressure oscillations originating from the jet, as can be seen in Figure 5(g). The timing of the ripples is nearly independent of z, showing that pressure information is communicated across the Maincap much faster that the flow dynamics of interest in the Maincap. The use of a quasi-static H-P description is thus justified.

For a pipe of circular-cross-section, the velocity profile for traditional H-P flow is given by

$$u(r) = \frac{\Delta P_{pipe}}{4\mu L}(R^2 - r^2), \tag{2}$$

where ΔP_{pipe} is the pressure difference over the length L of the pipe, μ is the dynamic viscosity, and r is the radial coordinate. To account for the evolution of the pressure and viscous forces in the Maincap, the flow speed is written as

$$u(r,z,t) = \frac{\Delta P_{main}(t)}{4\mu(z)L}(R^2 - r^2), \tag{3}$$

where $\Delta P_{main}(t)$ is the evolving pressure difference across the Maincap. Since viscous friction forces contribute linearly with the pipe length, the effect of the mixed gas composition can be modeled by using a viscosity of the form $\mu(z) = \mu_{H_2} + (z - z_0)\Delta\mu/L$, where $\Delta\mu \equiv \mu_{He} - \mu_{H_2}$, and $\mu_{He} = 18.7\ \mu$Pa s and $\mu_{H_2} = 8.7\ \mu$Pa s are the He and H_2 viscosities, respectively, at room temperature, and z is the longitudinal coordinate relative to the entrance of the device, and $z_0 = 4.6$ mm is the position of the start of the Maincap.

Assuming that the line-emission intensity is independent of r, the speed of the He-H_2 boundary seen in Figure 5 can thus be represented by the radially-averaged flow rate, given by

$$\bar{u}(z,t) = \frac{\Delta P_{main}(t)R^2}{8\mu(z)L} = \frac{1}{2}u_0(z,t), \tag{4}$$

where $u_0(z,t) \equiv u(0,z,t)$ is the maximum flow speed in the radial profile. To compare this expression to the data, however, requires information about $\Delta P_{main}(t)$. As Section III C will show, to get $\Delta P_{main}(t)$ requires an analysis of a pressure-divider effect caused by the junction between slot 1 and the capillary.

C. Pressure divider circuit

In the over-critical regime, the primary effect of the two fill slots, which connect to each other via the supply tubes, is to communicate pressure information from one side of the Maincap to the other, and thus lessen the pressure gradient driving the flow in this region. To model this effect, the device can be represented by a flow circuit (Fig. 6(a)), with each section acting like a flow resistor. The flow in each section then is described by Eq. (4), which can be written analogously to Ohm's law: $\Delta P = QZ$, where $Q \equiv A\bar{u}$ is the volumetric flow rate, A is the cross-sectional area, and $Z \equiv 8\pi(\mu L/A^2)$ is the component resistance (summarized in Table I, normalized to the resistance of the Midcap). The resistance of component combinations can then be calculated in the same way as for electrical circuits.

Since the resistance of the Maincap is large relative the other components, only a very small amount of the flow ($\sim$0.4% of the total) goes down the left branch of the loop. We thus approximate the effect of the loop by using an effective resistance, $Z_{eff} \approx Z_{slot1} + Z_{tube}$, which is approximately

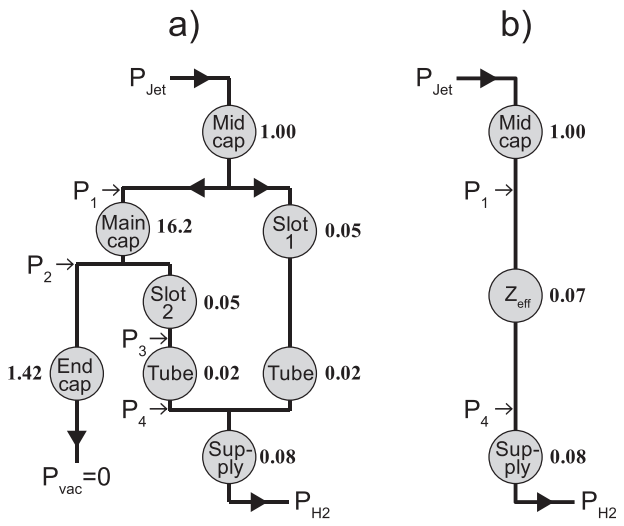

FIG. 6. (a) Circuit diagram modeling the effect of capillary fill slots on the dynamics of the hydrogen displacement in the Maincap. (b) Simplified circuit diagram combining elements of the loop into a single effective element.

TABLE I. Parameters describing the elements of the circuit, including resistances normalized to that of the Midcap, Z/Z_{Mid} and transit times, Δt, for gas to cross the elements for the range of conditions studied.

Element	L [mm]	R_{eff}[a]	Z/Z_{Mid}	Δt [ms][b]
Midcap	1.55	0.12	1.00	0.02–0.05
Maincap	25.1	0.12	16.2	2–12
Endcap	2.20	0.12	1.42	0.03–0.07
Slot	14	0.375	0.05	0.32–0.52
Tube	330	1.19	0.02	>15
Supply	1141	1.19	0.08	>50

[a]Effective radius defined by cross-sectional area of element.
[b]Ranges encompass values of P_{He} and P_{H_2} used here.

equal to the resistance of the right branch. The result is a simplified circuit, shown in Figure 6(b). The simplified circuit makes it is clear that the circuit acts as a pressure divider. For a one-gas, steady-state flow, the pressures across the Midcap and Maincap can thus be approximated by

$$\Delta P_{mid} \approx \frac{Z_{mid}}{Z_{mid}+Z_{eff}+Z_{supply}} \times (P_{jet}-P_{H_2}) \approx 0.87 \times (P_{jet}-P_{H_2}), \quad (5)$$

$$\Delta P_{main} \approx \frac{Z_{eff}}{Z_{mid}+Z_{eff}+Z_{supply}} \times (P_{jet}-P_{H_2}) \approx 0.06 \times (P_{jet}-P_{H_2}), \quad (6)$$

respectively. These expressions show that most of the pressure drop induced in the capillary by the jet in the over-critical condition is manifested across the Midcap, and only a small fraction, $\epsilon \equiv Z_{eff}/(Z_{mid}+Z_{eff}+Z_{supply}) \approx 0.06$, of it drives the flow in the Maincap. The effect of the jet evolution on the density profile is thus much stronger in the Midcap than in the Maincap. Nonetheless, the small Maincap pressure gradient can be observed as a 5–10% longitudinal variation in the line-intensity across the Maincap, most obvious in Fig. 5(c).

In principle, as He flows through the system, the resistances of the components change due to the difference in viscosity between He and H_2, modifying the behavior of the circuit. However, the estimates of the transit times, Δt, shown in Table I, obtained by integrating Eq. (4) for each component, show that the circuit evolution only affects the first ~0.5 ms of the Maincap dynamics, after which the circuit may be considered static. The impact of this evolution is minor, and while a more complete analysis accounting for this evolution is possible, it is beyond the scope of this paper.

The circuit analysis thus shows that the Maincap pressure drop should be expressed as $\Delta P_{main}(t) = \epsilon[P_{jet}(t) - P_{H_2}]$, where ϵ represents a pressure divider factor determined by the resistance ratio between the Midcap and slot 1. Using this expression and the jet-pressure information obtained above, the position of the boundary as a function of time, $z^*_{calc}(t)$, was then calculated by using $\bar{u}(z,t) = dz^*/dt$ to integrate Eq. (4)

$$\int_{z_0}^{z^*_{calc}(t)} \mu(z)dz = \frac{R^2}{8L}\int_{t_{crit}}^{t} \epsilon[P_{jet}(t') - P_{H_2}]dt'. \quad (7)$$

The results were then compared to the corresponding observed boundary positions, $z^*_{obs}(t)$, which were determined from the data in Fig. 5 by defining the boundary as the location within the He-H_2 boundary where the line brightness dropped to half of the maximum. Although both the He and H_2 emission line data gave similar results, the H_2 line was used exclusively for the analysis.

Figure 7 shows the comparison between $z^*_{calc}(t)$ and $z^*_{obs}(t)$ for $P_{He} = 30$ psi (gauge) and several capillary pressures. The observed positions are represented by the symbols, and the corresponding calculations based on $P_{jet}(t)$, are represented by the solid curves. Rather than use $\epsilon = 0.06$ obtained from the circuit analysis to do the comparison, ϵ was used as a fitting parameter which was optimized independently for each pressure value. The best fit values were then compared to the predicted value from the circuit analysis. This approach allowed a more precise comparison of the temporal dependences of $z^*_{calc}(t)$ and $z^*_{obs}(t)$, which was necessary for the analysis below. The best-fit values of ϵ were averaged for all combinations of $P_{He} \in \{10, 20, 30, 40, 50\}$ psi (gauge) and $P_{H_2} \in \{55, 70, 85, 100\}$ Torr, and resulted in $\langle \epsilon_{fit} \rangle = 0.108 \pm 0.025$, which agrees roughly with the circuit analysis. In addition, Figure 7 shows that the agreement between $z^*_{calc}(t)$ and $z^*_{obs}(t)$ is excellent, in both the shape and in absolute delay.

In order to determine the importance of the mixed-gas viscosity prescription, a separate analysis was then done of the $P_{H_2} = 100$ Torr case in which $\mu(z)$ was replaced with μ_{H_2}. Figure 7 (pink-dashed curve) shows that the agreement is, in fact, significantly worse for the pure-gas case. In particular, the pure-gas calculation has less curvature, which is precisely what should be expected. Since He has a greater viscosity than H_2, the flow should progressively slow down as more and more He enters the Maincap. This effect is absent in the pure-gas case. This analysis thus confirms the importance of viscosity in determining the flow.

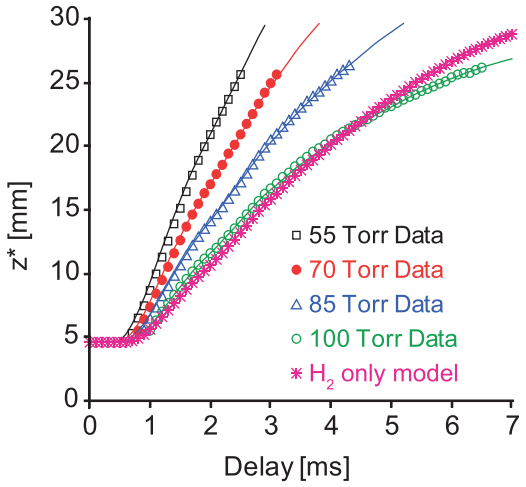

FIG. 7. Comparison of the measured and calculated boundary positions, z^*, for $P_{cap} = \{55, 70, 85, 100\}$ Torr and $P_{He} = 30$ psi (gauge). Measured values are represented by symbols and calculations using $P_{jet}(t)$, and fitting the values of ϵ is represented by curves with color corresponding to the symbols. A second calculation (pink stars) is done for the 100 Torr case where pure H_2 was assumed.

The H-P flow hypothesis thus appears well supported by both the quantitative agreement between the two estimates of ϵ as well as by the goodness of the fits in Figure 7. However, as will be described in Section III D, the parabolic radial flow profile inherent to the H-P based model presented so far conflicts with the high degree of sharpness of the edges in the longitudinal intensity distributions (Fig. 5) which define the boundaries between the He and H_2 regions in the Maincap. Resolution of this discrepancy required a detailed analysis of radial effects and diffusion at the He-H_2 interface (Fig. 8) which provided more information about the conditions within the capillaries.

D. Radial flow profile effects and diffusion

The gradient at the edges of the He and H_2 emission-line longitudinal intensity profiles represents a "boundary region" in which the radially-averaged composition of the gas is changing, due either to molecular intermixing or to interpenetration of the two flows. In the absence of mixing, the flow profile described in Eq. (2) implies a parabolic He-H_2 interface with a vertex that extends with time according to $z_{vertex}(t) = \int_{t_{crit}}^{t} u_0(z,t')dt' + z_0$ (Fig. 8(a)). Since the flow velocity at the wall is zero, the point where the parabola intersects the capillary should remain fixed at $z = z_0$. As a result, the He and H_2 concentrations, averaged over the radial profile, should vary linearly with distance, $z' \equiv z - z_0$, between z_0 and $z_{vertex}(t)$ (Fig. 8(b)). In this picture, the boundary region should thus always reach z_0. Inspection of the data in Fig. 8(c), however, shows that the boundary region (delineated by the dashed lines) can be well separated from $z_0 \approx 5$ mm.

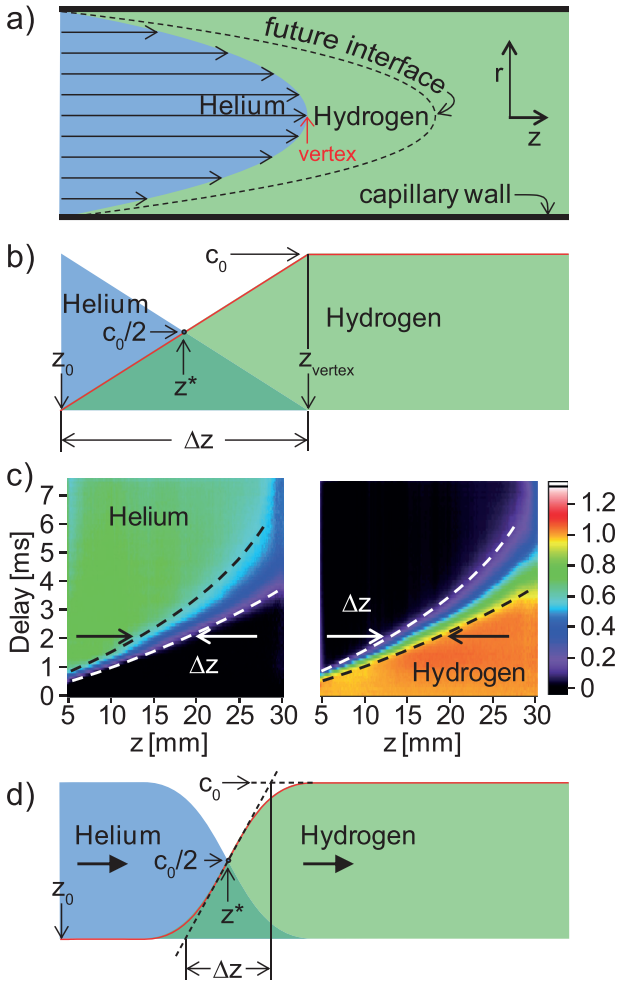

FIG. 8. Helium-hydrogen interface. (a) Diagram of the He-H_2 interface for H-P flow, depicting the gas distributions in an r-z slice of the capillary. (b) Expected radially-averaged concentrations of He and H_2 for H-P flow case depicted in (a). (c) Sample data showing the evolution of the longitudinal distributions of He (left) and H_2 (right). The dashed lines indicate the edges of the boundary region. (d) Diagram showing a snapshot of the longitudinal intensity distributions of the He and H_2 lines, overlapped. The position of the interface is defined as the location where the line brightness is half of the maximum, corresponding to a radially-integrated gas concentration that is half of maximum.

To quantify these effects, we define a gradient scale-length for the boundary by $\Delta z \equiv c_0/\partial_z c(z^*)$, where $c(z)$ is the longitudinally-varying line brightness (correlated to the radially-averaged H_2 concentration) and c_0 is the brightness of the H_2 emission line corresponding to a concentration of 100%. The location, z^*, of the boundary is then defined by $c(z^*) \equiv c_0/2$, and the gradient in the brightness at that location is $\partial_z c(z^*)$ (Fig. 8(d)). To compare the measured scale-lengths with the H-P model, we used the normalized scale-length, $\Delta z/z^{*\prime}$, where $z^{*\prime} \equiv z^* - z_0$. Since the normalized gradient scale length in the H-P model is a constant ($\Delta z/z^{*\prime} = 2$—see Fig. 8(b)), the measured values of $\Delta z/z^{*\prime}$ could be averaged over delay as well as P_{H_2} (Fig. 9(a)). The fact that the measured values are significantly less than 2 is equivalent to the statement above that the boundary is separated from the origin, as depicted in Figs. 8(c) and 8(d).

The strong dependence of $\Delta z/z^{*\prime}$ on P_{He} in Figure 9(a) indicates that another mechanism is most likely at play. The obvious choice is diffusion. To test this hypothesis, Δz data for all P_{He} and P_{H_2} were combined in a plot versus $t - t_{crit}$ (Fig. 9(b)). The plot shows that the temporal dependence of the gradient scale-length is fit very well by a function describing diffusive mixing of He and H_2 at the interface: $\Delta z = \sqrt{4\pi D t}$. The diffusion coefficient, D, was then plotted as a function of capillary pressure and compared with known values for the inter-diffusion coefficient of a binary He-H_2 mixture,[24] as well as for the self-diffusion coefficients for pure helium[25] and pure hydrogen[26] (Fig. 9(c)). The good agreement in both value and dependence show that the observed gradients are well explained by diffusive mixing. The dependence of $\Delta z/z^{*\prime}$ on P_{He} in Figure 9(a) can thus be explained as resulting from the dependence of the flow speed on the driving pressure, which affects the amount of time available for diffusive mixing.

The success of the diffusive mixing model, however, only exacerbates the discrepancy of the gradient analysis with the H-P flow model. To estimate the contribution to the gradient from the radial flow profile, $(\Delta z/z^{*\prime})_{flow}$, the contribution from diffusion, $(\Delta z/z^{*\prime})_{diff}$ must first be removed. To do this, we used the value of $\Delta z/z^{*\prime}$ from Figure 9(a) corresponding to the least amount of diffusion as an upper bound to $(\Delta z/z^{*\prime})_{flow}$. The flow contribution is dependent only on the distance traveled by the interface, and not on the time taken to traverse the distance, while the diffusion contribution is dependent only on time. Therefore, the case with the

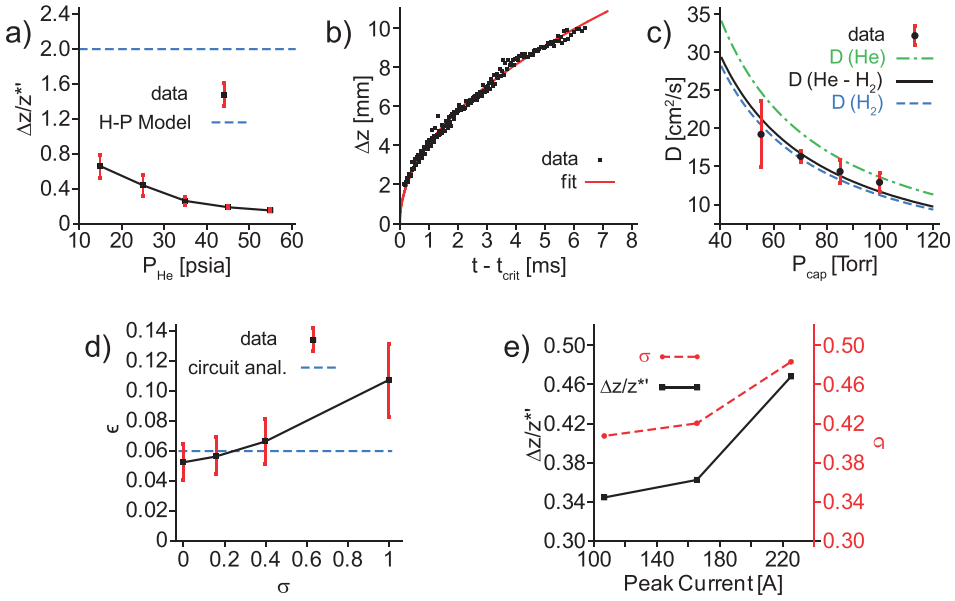

FIG. 9. (a) Measured normalized gradient scale-lengths vs P_{He} (black dots) and prediction from H-P flow (blue-dashed line). (b) Measurement of diffusion coefficient by fitting gradient scale-length vs time relative to t_{crit}. (c) Comparison of measured diffusion coefficients vs P_{cap} (black dots) against known values of interdiffusion coefficient for a He-H_2 binary mixture (black curve) and self diffusion coefficients of He and H_2 (green-dashed and blue-dotted curves, respectively). (d) Fit values for ϵ as a function of σ. Each point corresponds to an average over P_{He} and P_{H_2} values. (e) Normalized gradient scale-length (black line) and corresponding σ values (red-dashed curve) vs peak discharge current. Note: Lines connecting data points in figures (a), (d), and (e) are only meant to guide the eye.

highest flow velocity, the shortest time for the boundary to move across the capillary and therefore the least amount of diffusion represents an upper bound to the contribution from the flow profile. This case corresponds to the highest P_{He} and the smallest value of $\Delta z/z^{*\prime}$, so we can estimate $(\Delta z/z^{*\prime})_{flow} \leq 0.16$, which is much smaller than the predicted value of 2.

Since the dynamics of the boundary region is dictated by the radial flow profile, two potential explanations exist for the discrepancy: (1) the radial flow profile is significantly flatter than parabolic or (2) the emission-line intensity is radially non-uniform. Since the importance of viscosity (which necessitates a parabolic flow profile) in describing the propagation of the He-H_2 boundary was confirmed, the second explanation is indicated. In this case, the observations would more strongly weight the radial section of the flow profile corresponding to the greatest temporally-integrated emission of light. This boundary analysis may thus provide a measure of information about the radial distribution of light emission from the capillary even though the imaging system was incapable of directly resolving radial features (and thus only yielded radially-averaged measurements).

To estimate the magnitude of the radial-weighting effect, the H-P model was revised to include only the central subset of the radial distribution defined by $r \leq r_{max}$. The contribution to the normalized gradient scale-length from the radial flow profile within r_{max} is then given by

$$\frac{\Delta z}{z^{*\prime}}(\sigma) = \frac{2\sigma}{2-\sigma}, \tag{8}$$

where $\sigma \equiv (r_{max}/R)^2$ corresponds to the effective fractional area of the capillary cross-section contributing to the measurement. By selecting only the central portion of the flow profile, the range of encompassed flow speeds is reduced, which in turn reduces the gradients in the boundary and increases the average speed according to

$$\bar{u} = \frac{1}{2}u_0(2-\sigma). \tag{9}$$

The value of σ therefore has an impact on the best fit value of ϵ by adjusting the calculated flow rate for a given pressure gradient. Best-fit values of ϵ were determined for a range of σ values between 0 and 1 (Fig. 9(d)). The figure shows that by reducing σ below 1, the agreement between the best-fit value of ϵ and the value of 0.06 determined from the pressure-divider circuit analysis is improved. The best agreement occurs at $\sigma = 0.22$, which corresponds to $\Delta z/z^{*\prime}(\sigma) = 0.25$, which is not far from upper-limit value of 0.16 determined above from Figure 9(a). Thus, the interpretation that only the central portion of the radial flow profile contributes to the measurement not only explains the discrepancy in the gradient scale length but also improves the agreement between the calculated and measured positions of the He-H_2 boundary.

It is likely that the radial distribution of light emission is connected to the current dynamics during the discharge, raising the interesting possibility that something may be learned from the boundary analysis about the radial current profile or about the mechanisms involved in the emission. As a preliminary test along these lines, the peak current of the discharge was varied to see if any effect on $\Delta z/z^{*\prime}$ could be observed. Figure 9(e) (black solid line) shows that increasing the peak current from 110 A to 220 A indeed increased the normalized scale length by an amount of the same order as the flow contribution estimated from Figure 9(a), suggesting that the radial distribution of light emission may depend on discharge current.

E. Operation and design considerations

The analysis presented here provides a strategy for designing and tuning the device to obtain the desired longitudinal density profile. In the original design concept, a localized high-density region connects directly to a longer, uniform-density region. We have shown that to achieve this "critical profile," the device must be operated at the critical condition, and that P_{He} cannot be used to tune the peak jet density without affecting the density gradients in the jet

vicinity. Since the evolution of the longitudinal density profile follows a similar pattern during the ramp-up of pressure in the jet for different values of P_{He}, the choice of P_{He} primarily affects how fast the evolution coordinate changes and the maximum pressure achievable. This result identifies the jet timing as a more useful tuning knob than jet backing pressure for achieving the desired profile.

A key design parameter of the critical profile is the ratio of the electron density in the jet to that in the capillary, $n_{jet}(t_{crit})/n_{cap}$, which is set by the degree of expansion of the jet gas in the nozzle. This ratio can be determined by using the assumption of isentropic expansion ($P/\rho^{\gamma} = const$) in conjunction with the ideal gas law and the critical condition, $P_{jet}(t_{crit}) = P_{cap}$:

$$\frac{n_{jet}}{n_{cap}}(t_{crit}) = \left(\frac{P_{jet}}{P_{He}}\right)^{-\frac{\gamma-1}{\gamma}}. \tag{10}$$

Using the calibration $P_{jet}/P_{He} = 0.085$ from the jet characterization in Section III A gives $n_{jet}(t_{crit})/n_{cap} \approx 2.7$. This estimate assumes that both the capillary and the He at the source are at room temperature, and do not take into account density or pressure structure within the jet which could be important.

Operating away from the critical condition provides a greater range of options. In this case, jet timing can be used as a knob for tuning the longitudinal density profile in the region connecting the jet to the rest of the capillary, which has been shown to sensitively affect electron injection in the accelerator.[13] The gradient in this region can be tuned from negative to positive while minimally affecting the rest of the capillary. These longitudinal density gradients are important because they control the phase velocity of the plasma accelerating structures relative to the electrons, which affects both electron injection and subsequent acceleration.[13] The density gradients in the Midcap and Maincap can be quantitatively estimated by applying the ideal gas law to the pressure analysis described above and using the estimates of the jet and capillary temperatures

$$\left[\frac{\partial n}{\partial z}(t)\right]_{Mid}^{t\le t_{crit}} \approx \frac{P_{cap} - P_{jet}(t)}{k_B T_{cap} L_{Mid}}, \tag{11}$$

$$\left[\frac{\partial n}{\partial z}(t)\right]_{Mid}^{t>t_{crit}} \approx \frac{(1-\epsilon)P_{cap} - \left(\frac{T_{cap}}{T_{jet}} - \epsilon\right)P_{jet}(t)}{k_B T_{cap} L_{Mid}}, \tag{12}$$

$$\left[\frac{\partial n}{\partial z}(t)\right]_{Main}^{t\le t_{crit}} \approx 0, \tag{13}$$

$$\left[\frac{\partial n}{\partial z}(t)\right]_{Main}^{t>t_{crit}} \approx \frac{\epsilon\left[P_{cap} - P_{jet}(t)\right]}{k_B T_{cap} L_{Main}}, \tag{14}$$

where L_{Mid} and L_{Main} are the lengths of the Midcap and Maincap, respectively.

In the over-critical regime, temperature gradients can play a significant role in the Midcap, since the cold jet gas leaking into the room-temperature structure takes time to heat up. The timescale for the leaking gas to thermalize with the capillary based on radial heat conduction ($\sim 35\mu s$) is similar to the timescale for the gas to traverse the Midcap ($\sim 30\mu s$). The temperature difference between the jet and capillary gases will therefore accentuate the density gradients in the Midcap. In the Maincap, however, the thermalization timescale is much shorter than the transit timescale, and the gas can be considered to be fixed at the (room) temperature of the sapphire. In this case, pressure variations can be directly interpreted as density variations. As temperature is clearly an important factor in determining the density, it would be beneficial to supplement the measurements presented here with direct measurements of the temperature.

Over-critical operation, using different gas-species for the jet and capillary carries the additional consequence of producing a Maincap section with mixed composition, the impacts of which are not known. Across the interface, the molecular number density is preserved, because both temperature and pressure are matched, however the electron density after ionization will depend on the number of ionization stages for each molecule. For a He-H_2 interface, no electron density gradient is expected at the interface, but for other species combinations, the interface could present a method for generating sub-mm electron-density jumps with tunable position. For high-repetition-rate applications, over-critical operation with two species is also problematic since the jet gas becomes trapped in between the slots, with a concentration that evolves on the diffusion timescale, which can be many milliseconds.

As a final note, the speed of the He-H_2 boundary in the Maincap provides an additional benefit as a diagnostic of ablative damage to the capillary structures. Since the dynamics of this device is sensitively determined by the shape of the jet nozzle, which sets $P_{jet}(t)$ and T_{jet}, and by the resistance of the Midcap section, which sets ϵ, any ablative damage to the jet and Midcap from the high-intensity laser causes dramatic changes in the speed of the flow through the Maincap. This change is necessarily accompanied by significant changes in both the jet density and Midcap gradients.

IV. CONCLUSIONS

We have shown that it is possible to resolve the gas dynamics and pressure gradients in a longitudinally-structured LPA target composed of a capillary discharge waveguide and an embedded supersonic jet, providing information critical for proper tuning of the accelerator. The dynamics are captured by using helium in the jet and hydrogen in the capillary and spatially resolving individual emission lines of the recombination light associated with the two gases. The discharge acts like a strobe that allows capture of the spatial distributions of the gases as a function of delay after the jet is fired. We used this technique to develop a phenomenological description of the device behavior and quantify the pressure evolution in the jet and capillary.

In particular, a transducer was developed for the jet pressure, and a diagnostic of the pressure balance between the jet and the capillary was identified. These two developments allowed calibration of the jet pressure evolution and characterization of the embedded supersonic nozzle. The

determination of the jet pressure enabled modeling of the interaction between the jet and capillary gases which allowed quantification of density gradients in the device and of their evolution.

The characterization of the pressure dynamics, which has not been directly accessible previously, as well as the development of models describing the device behavior together provide a detailed prescription for controlling the evolution and longitudinal distribution of the gas density. In particular, jet timing is identified as an effective method to tune the density gradients at the jet-capillary junction and in the capillary as well as the longitudinal composition of the capillary gas.

ACKNOWLEDGMENTS

The authors would like to acknowledge Dr. Max Zolotorev for many valuable conversations. This work was supported by the Director, Office of Science, Office of High Energy Physics, of the U.S. DOE under Contract No. DE-AC02-05CH11231.

[1]T. Tajima and J. M. Dawson, "Laser electron accelerator," Phys. Rev. Lett. **43**, 267 (1979).
[2]W. Leemans and E. Esarey, "Laser-driven plasma-wave electron accelerators," Phys. Today **62**(3), 44 (2009).
[3]E. Esarey, C. B. Schroeder, and W. P. Leemans, "Physics of laser-driven plasma-based electron accelerators," Rev. Mod. Phys. **81**, 1229 (2009).
[4]T. Katsouleas, "Electrons hang ten on laser wake," Nature **431**, 515 (2004).
[5]V. Malka, J. Faure, Y. A. Gauduel, E. Lefebvre, A. Rousse, and K. Ta Phuoc, "Principles and applications of compact laser-plasma accelerators," Nat. Phys. **4**, 447 (2008).
[6]F. Albert, A. G. R. Thomas, S. P. D. Mangles, S. Banerjee, S. Corde, A. Flacco, M. Litos, D. Neely, J. Vieira, Z. Najmudin, R. Bingham, C. Joshi, and T. Katsouleas, "Laser wakefield accelerator based light sources: Potential applications and requirements," Plasma Phys. Controlled Fusion **56**, 084015 (2014).
[7]M. Fuchs, R. Weingartner, A. Popp, Z. Major, S. Becker, J. Osterhoff, I. Cortrie, B. Zeitler, R. Hörlein, G. D. Tsakiris, U. Schramm, T. P. Rowlands-Rees, S. M. Hooker, D. Habs, F. Krausz, and F. Grüner, "Laser-driven soft-X-ray undulator source," Nat. Phys. **5**, 826 (2009).
[8]S. Kneip, C. McGuffy, J. L. Martins, S. F. Martins, C. Bellei, V. Chvykov, F. Dollar, R. Fonseca, C. Huntington, G. Kalintchenko, A. Maksimchuk, S. P. D. Mangles, T. Matsuoka, S. R. Nagel, C. A. J. Palmer, J. Schreiber, K. Ta Phuoc, A. G. R. Thomas, V. Yanovsky, L. O. Silva, K. Krushelnick, and Z. Najmudin, "Bright spatially coherent synchrotron X-rays from a table-top source," Nat. Phys. **6**, 980 (2010).
[9]Z.-H. He, A. G. R. Thomas, B. Beaurepaire, J. A. Nees, B. Hou, V. Malka, K. Krushelnick, and J. Faure, "Electron diffraction using ultrafast electron bunches from a laser-wakefield accelerator at kHz repetition rate," Appl. Phys. Lett. **102**, 064104 (2013).
[10]A. D. Roberts, C. G. R. Geddes, N. H. Matlis, K. Nakamura, J. P. O'Neil, B. H. Shaw, S. Steinke, J. van Tilborg, and W. P. Leemans, "Measured Bremsstrahlung photonuclear production of ^{99}Mo (^{99m}Tc) with 34 MeV to 1.7 GeV electrons," Appl. Rad. Isotopes **96**, 122 (2015).
[11]W. P. Leemans, B. Nagler, A. J. Gonsalves, Cs. Tóth, K. Nakamura, C. G. R. Geddes, E. Esarey, C. B. Schroeder, and S. M. Hooker, "GeV electron beams from a centimetre-scale accelerator," Nat. Phys. **2**, 696 (2006).
[12]W. P. Leemans, A. J. Gonsalves, H.-S. Mao, K. Nakamura, C. Benedetti, C. B. Schroeder, Cs. Tóth, J. Daniels, D. E. Mittelberger, S. S. Bulanov, J.-L. Vay, C. G. R. Geddes, and E. Esarey, "Multi-GeV electron beams from capillary-discharge-guided subpetawatt laser pulses in the self-trapping regime," Phys. Rev. Lett. **113**, 245002 (2014).
[13]A. J. Gonsalves, K. Nakamura, C. Lin, D. Panasenko, S. Shiraishi, T. Sokollik, C. Benedetti, C. B. Schroeder, C. G. R. Geddes, J. van Tilborg, J. Osterhoff, E. Esarey, Cs. Tóth, and W. P. Leemans, "Tunable laser plasma accelerator based on longitudinal density tailoring," Nat. Phys. **7**, 862 (2011).
[14]L. Schaper, L. Goldberg, T. Kleinwächter, J.-P. Schwinkendorf, and J. Osterhoff, "Longitudinal gas-density profilometry for plasma-wakefield acceleration targets," Nucl. Instrum. Methods, Phys. Res., Sect. A **740**, 208 (2014).
[15]M. Kalal and K. A. Nugent, "Abel inversion using fast Fourier transforms," Appl. Opt. **27**, 1956 (1988).
[16]M. Krishnan, K. W. Elliott, C. G. R. Geddes, R. A. Mourik, W. P. Leemans, H. Murphy, and M. Clover, "Electromagnetically driven, fast opening and closing gas jet valve," Phys. Rev. ST Accel. Beams **14**, 033502 (2011).
[17]J. D. Anderson, *Modern Compressible Flow With Historical Perspective*, 3rd ed. (McGraw-Hill, 2002).
[18]S. Varoutis, D. Valougeorgis, O. Sazhin, and F. Sharipov, "Rarefied gas flow through short tubes into vacuum," J. Vac. Sci. Technol. A **26**, 228 (2008).
[19]F. M. Sharipov and V. D. Seleznev, "Rarefied as flow through a long tube at any pressure ratio," J. Vac. Sci. Technol. A **12**, 2933 (1994).
[20]N. H. Matlis, A. J. Gonsalves, S. Steinke, J. van Tilborg, B. Shaw, C. G. R. Geddes, and W. P. Leemans, "Transient behavior of a supersonic 3D micronozzle with an intersecting capillary," J. Appl. Phys. (submitted).
[21]C. N. Woods, "A study of gas dynamics under Poiseuille conditions: A comparison of the fluid equations and DSMC," Senior thesis (Brigham Young University, 2008).
[22]A. P. Willis, J. Peixinho, R. R. Kerswell, and T. Mullin, "Experimental and theoretical progress in pipe flow transition," Philos. Trans. R. Soc. A **366**, 2671 (2008).
[23]D. Fargie and B. W. Martin, "Developing laminar flow in a pipe of circular cross-section," Proc. R. Soc. London, Ser. A **321**, 461 (1971).
[24]T. R. Marrero and E. A. Mason, "Gaseous diffusion coefficients," J. Phys. Chem. Ref. Data **1**, 3 (1972).
[25]J. Kestin, K. Knierim, E. A. Mason, B. Najafi, S. T. Ro, and M. Waldman, "Equilibrium and transport of the nobel gases and their mixtures at low density," J. Phys. Chem. Ref. Data **13**, 229 (1984).
[26]S. Mathur and S. C. Saxena, "Relations between thermal conductivity and diffusion coefficients of pure and mixed polyatomic gases," Proc. Phys. Soc. **89**, 753 (1966).
[27]See http://www.engineering.com/calculators/isentropic_flow_relations.htm for "Isentropic Flow Relations Calculator" (last accessed: January 15, 2015).